ChemComm

FEATURE ARTICLE

View Article Online
View Journal | View Issue

Cite this: *Chem. Commun.*, 2018, **54**, 5943

Electrocatalytic and photocatalytic hydrogen evolution integrated with organic oxidation

Bo You, † Guanqun Han† and Yujie Sun *

Renewable energy-driven hydrogen production from electrocatalytic and photocatalytic water splitting has been widely recognized as a promising approach to utilize green energy resources and hence reduces our dependence on legacy fossil fuels as well as alleviates net carbon dioxide emissions. The realization of large-scale water splitting, however, is mainly impeded by its slow kinetics, particularly because of its sluggish anodic half reaction, the oxygen evolution reaction (OER), whose product O_2 is ironically not of high value. In fact, the co-production of H_2 and O_2 in conventional water electrolysis may result in the formation of explosive H_2/O_2 gas mixtures due to gas crossover and reactive oxygen species (ROS); both pose safety concerns and shorten the lifetimes of water splitting cells. With these considerations in mind, replacing the OER with thermodynamically more favorable organic oxidation reactions is much more preferred, which will not only substantially reduce the voltage input for H_2 evolution from water and avoid the generation of H_2/O_2 gas mixtures and ROS, but also possibly lead to the co-production of value-added organic products on the anode. Indeed, such an innovative strategy for H_2 production integrated with valuable organic oxidation has attracted increasing attention in both electrocatalysis and photocatalysis. This feature article showcases the most recent examples along this endeavor. As exemplified in the main text, the oxidative transformation of a variety of organic substrates, including alcohols, ammonia, urea, hydrazine, and biomass-derived intermediate chemicals, can be integrated with energy-efficient H_2 evolution. We specifically highlight the importance of oxidative biomass valorization coupled with H_2 production, as biomass is the only green carbon source whose scale is comparable to fossil fuels. Finally, the remaining challenges and future opportunities are also discussed.

Received 6th March 2018,
Accepted 3rd May 2018

DOI: 10.1039/c8cc01830h

rsc.li/chemcomm

1. Introduction

The continuous economic development and increasing global population necessitate the steady growth of energy production. As the current energy sector is highly dependent on fossil fuels, including coal, oil, and natural gas, their limited reserves pose

Department of Chemistry and Biochemistry, Utah State University, Logan, Utah 84322, USA. E-mail: yujie.sun@usu.edu; Fax: +1-435-797-3390; Tel: +1-435-797-7608

† These authors contributed equally.

Bo You

Dr Bo You received his BS degree in Chemistry from Heilongjiang University in 2008 and his PhD degree under the supervision of Prof. Zhaoxiang Deng at the University of Science and Technology of China in 2014. Subsequently, he conducted a postdoctoral research in Prof. Yujie Sun's group at Utah State University. His research interest is interface catalysis for advanced renewable energy (ICARE).

Guanqun Han

Guanqun Han received her BS degree in Polymer Materials and Engineering from the Qingdao University of Science and Technology in 2012 and her MS degree in Chemistry from the China University of Petroleum (East China) in 2016. Since then, she has been pursuing her PhD degree at Utah State University under the supervision of Prof. Yujie Sun. Her research interests include inexpensive heterogeneous catalysts for H_2 evolution and organic upgrading.

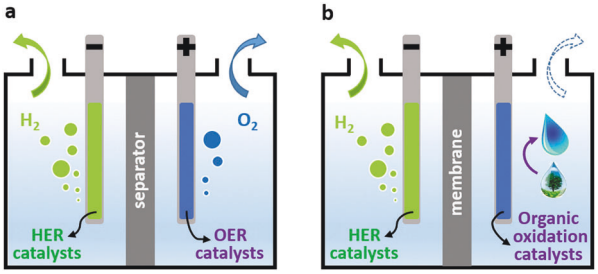

Fig. 1 Design of (a) a conventional water splitting electrolyzer and (b) a novel electrolyzer integrating H_2 evolution with organic oxidation.

a risk for our long-term development.[1–3] In addition, the adverse effect of fossil fuel utilization has been well manifested by its detrimental impact on the environment, climate, and health of our planet. Consequently, intense research efforts have been focused on the capture, conversion, storage, and utilization of sustainable and clean energy resources, like solar light and wind.[4,5] It has been estimated that the energy of solar irradiation on the Earth's surface for 80 min is sufficient to meet the global energy demands for an entire year based on the current consumption rate.[2] To address the intermittency issue of renewable energies like solar irradiation, electrocatalytic and photocatalytic H_2 generation from water have been considered as attractive approaches for renewable energy storage in the form of chemical bonds.[6–8] In this case, the produced H_2 can be stored and later used on demand *via* hydrogen fuel cells. Additionally, H_2 is also a commodity chemical in the chemical industry.

As shown in Fig. 1a, conventional water electrolysis is usually conducted in strongly acidic electrolytes with noble metal-based catalysts (*e.g.*, Pt for the HER, and IrO_2 or RuO_2 for the OER) and a proton exchange membrane (PEM) or in alkaline media using transition metal-based catalysts (*e.g.*, Ni for the HER and stainless steel for the OER) and diaphragms.[9,10] In both cases, the H_2 and O_2 evolution reactions (HER and OER) are strictly coupled, which may lead to the formation of explosive H_2/O_2 mixtures due to gas crossover.[11–13] Gas crossover not only poses safety concerns but also reduces the energy conversion efficiency as the crossed O_2 will be reduced back to water (acidic media) or hydroxide anions (alkaline media) on the cathode side.[9] In addition, the coexistence of H_2/O_2 gas mixtures and electrocatalysts may result in the formation of reactive oxygen species (ROS), which can degrade the membrane and thus shorten the lifetimes of electrolyzers.[11] Another well-known limitation is that the four-electron/four-proton nature of the OER requires a much higher overpotential input than that of the HER to afford the same current density, while the product O_2 is not very valuable. In fact, the voltage input for practical water splitting electrolyzers is always substantially larger than the standard thermodynamic potential of 1.23 V.

An alternative strategy for H_2 production from water is to replace the challenging but less valuable OER with thermodynamically favourable and economically more attractive organic oxidation reactions. Such a novel strategy will not only lower the voltage input and exclude the formation of H_2/O_2 gas mixtures and ROS, but also produce more valuable organic products on the anode, maximizing the return of energy investment (Fig. 1b).

This Feature Article aims to present an overview of recent progress in electrocatalytic and photocatalytic H_2 generation integrated with various organic oxidation reactions. A diverse array of organic substrates could be employed in this new strategy, ranging from alcohols,[14–18] ammonia,[19–21] urea,[22–25] and hydrazine[26–28] to biomass-derived intermediate compounds[29–34] and others.[35–37]

2. Electrocatalytic HER integrated with organic oxidation

Even though the thermodynamic potential of water splitting is only 1.23 V under standard conditions, a cell voltage of 1.6–2.0 V is typically required to achieve a current density larger than 10 mA cm^{-2} in practical electrolyzers. Consequently, appreciable production of H_2 can only be achieved with an electrical energy consumption exceeding 45 kW h kg^{-1} H_2. Because of the much lower standard thermodynamic potentials of alcohol oxidation reactions than that of the OER, Vizza *et al.* demonstrated that it was feasible to replace the OER with alcohol oxidation to produce H_2 with a voltage less than 1 V, using palladium nanoparticles deposited on three-dimensional titania nanotube arrays (Pd/TNTA-web) as the anode electrocatalysts (Fig. 2a and b).[14] For the preparation of Pd/TNTA-web, a commercial titanium non-woven sintered web support was anodized and annealed to form finely distributed titania nanotube arrays (TNTAs), as confirmed by the scanning electron microscopy (SEM) image (Fig. 2c). Subsequently, a dipping–chemical reduction procedure was employed to deposit Pd nanoparticles. The SEM image in Fig. 2d clearly confirms the homogeneous Pd distribution on the inner surfaces of the TNTAs. The TNTAs had

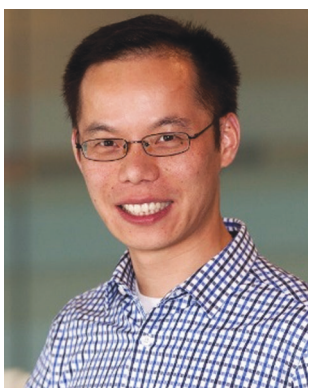

Yujie Sun

Dr Yujie Sun received his BS degree in Chemistry from Fudan University in 2005. He then pursued graduate studies in inorganic photochemistry with Prof. Claudia Turro at the Ohio State University and received his PhD degree in 2010. Subsequently, he joined the group of Prof. Chris Chang at the University of California, Berkeley, and the Lawrence Berkeley National Laboratory for postdoctoral studies. In 2013, Yujie started his independent career as an assistant professor at Utah State University. His group is interested in developing and understanding inexpensive materials and complexes for energy catalysis and biomedical applications.

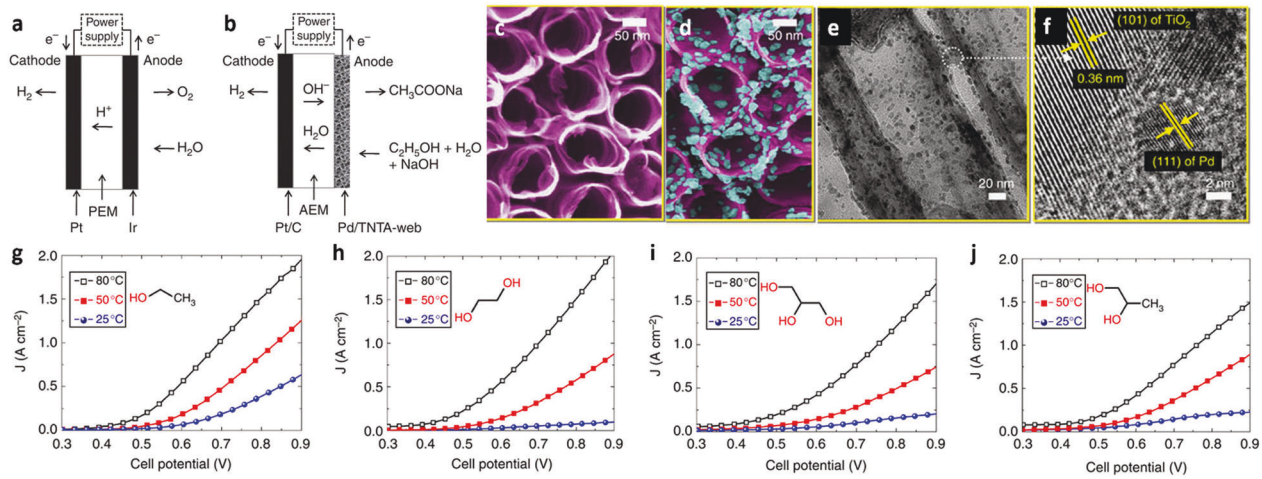

Fig. 2 Schematic of (a) PEM water electrolysis and (b) proposed alkaline water electrolysis. SEM images of (c) the bare 3D TNTA electrode support and (d) Pd/TNTA-web. (e) TEM and (f) HR-TEM images of Pd/TNTA-web. (g–j) Polarization curves for Pd/TNTA-web-based water electrolysis in 2 M NaOH solutions of (g) 2 M ethanol, (h) 2 M ethylene glycol, (i) 2 M glycerol, and (j) 2 M 1,2-propanediol at different temperatures. Reproduced from ref. 14 with permission from Springer Nature, copyright 2014.

an inner diameter of 100 nm with a wall thickness of 10 nm, and the Pd nanoparticles had an average particle size of ~13 nm (Fig. 2e). High-resolution transmission electron microscopy (HR-TEM) characterization also revealed the crystalline lattices of both anatase and metallic Pd (Fig. 2f), further confirming the successful formation of Pd/TNTA-web. A two-electrode alkaline water electrolyzer was assembled using Pd/TNTA-web as the anode and Pt/C on carbon cloth as the cathode in 2 M NaOH (Fig. 2b). Fig. 2g shows the typical polarization curves obtained at 25, 50, and 80 °C with 2 M ethanol. It is apparent that the output current density at a cell potential of 0.9 V at 80 °C (1.95 A cm^{-2}) is more than three times higher than that at 25 °C (0.51 A cm^{-2}), mainly due to the enhanced kinetics of ethanol oxidation with temperature increase. Similar results were obtained for other alcohols including ethylene glycol (Fig. 2h), glycerol (Fig. 2i) and 1,2-propanediol (Fig. 2j). It was calculated that the use of ethanol for H_2 production (18.5 kW h kg^{-1} H_2) results in an electrical energy saving of 26.5 kW h kg^{-1} H_2. Moreover, these alcohols can be produced from the fermentation of biomass or steam reforming of cellulosic materials with reasonably low energy cost,[14] and the corresponding products of organic acids are more valuable than O_2.[34b] However, the utilization of Pd and Pt-based electrocatalysts inevitably leads to a high cost of the electrolyzer.

With this consideration in mind, we reasoned that it is economically more appealing to explore first-row transition metal-based electrocatalysts. Our group recently reported a 3D hierarchically porous nickel electrocatalyst (hp-Ni) for such an integrated water electrolysis.[33] The hp-Ni electrocatalyst was prepared by a facile template-free cathodic electrodeposition of highly porous Ni microspheres on a nickel foam at 3.0 A cm^{-2} for 500 s. The SEM images in Fig. 3a indicated the 3D hierarchically macroporous nature of hp-Ni with a pore size of several hundred micrometers and abundant smaller macropores on the interconnected walls. Such a hierarchically porous structure

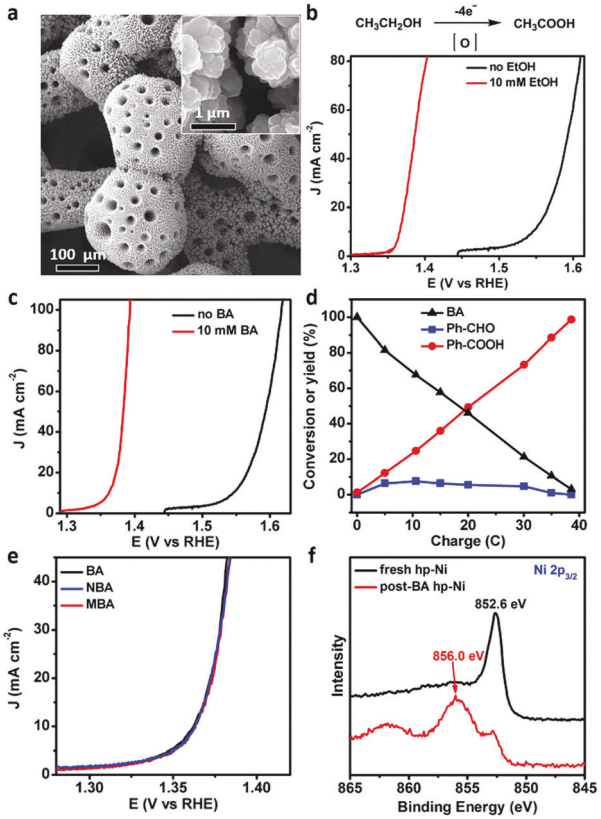

Fig. 3 (a) SEM images of hp-Ni. (b) LSV curves for the oxidation of ethanol (EtOH, 10 mM) and water in 1.0 M KOH at 2 mV s^{-1}. (c) LSV curves of the oxidation of benzyl alcohol (BA, 10 mM) and water in 1.0 M KOH at 2 mV s^{-1}. (d) Benzyl alcohol conversion and product yield over passed charge during electrocatalysis at 1.423 V *vs.* RHE. (e) LSV curves of the oxidation of 10 mM benzyl alcohol (BA), 4-methylbenzyl alcohol (MBA), and 4-nitrobenzyl alcohol (NBA) on hp-Ni at 2 mV s^{-1} in 1.0 M KOH. (f) High-resolution Ni $2p_{3/2}$ XPS spectra of the fresh and post-BA hp-Ni electrocatalysts. Reproduced from ref. 33 with permission from American Chemistry Society, copyright 2017.

is believed to facilitate the accessibility of catalytically active sites and mass transport for improved electrocatalytic performance.[38] Fig. 3b plots the linear sweep voltammetry (LSV) curves of the oxidation of ethanol and water on hp-Ni in 1.0 M KOH. Upon addition of 10 mM ethanol, the catalytic onset potential shifted from 1.51 V to 1.35 V *vs.* RHE and a substantial anodic current density was observed within 1. 4 V *vs.* RHE, indicative of ethanol oxidation being easier than the OER. In order to demonstrate the versatility of hp-Ni, we further extended the organic substrate group to benzyl alcohol (BA). A similar cathodic shift of the LSV curve was observed once BA was added to the electrolyte (Fig. 3c). Long-term electrolysis was conducted at 1.423 V *vs.* RHE, where no water oxidation would occur. The concentration evolutions of BA and its oxidation products were analysed by high-performance liquid chromatography (HPLC) and are plotted in Fig. 3d, clearly indicating an increase of benzoic acid but a decrease of BA over passed charge. As an initial endeavour to explore the electronic effect on alcohol oxidation catalyzed by hp-Ni, two derivatives of benzyl alcohol with electron-withdrawing (4-nitrobenzyl alcohol, NBA) and -donating (4-methylbenzyl alcohol, MBA) substituents at the *para* position were subjected to similar electrocatalytic oxidation on hp-Ni. Interestingly, both LSV curves of these two new substrates took off at quite similar potentials in comparison to that of the parent benzyl alcohol (Fig. 3e), suggesting that the catalytic onset potentials of these alcohol oxidation reactions are primarily determined by the potential to achieve the desirable oxidation state of hp-Ni, rather than the intrinsic thermodynamics of alcohol oxidation. Such an integrated electrolyzer required a voltage of 1.58 V to afford 50 mA cm^{-2}, nearly 220 mV smaller than that of pure water splitting and other nonprecious electrocatalyst-based water electrolysis at the same current density.[1c] Post-electrolysis characterization of hp-Ni after stability tests (named post-BA hp-Ni) demonstrated its partial oxidation on the catalyst surface. For example, the high-resolution Ni $2p_{3/2}$ XPS spectrum for post-BA hp-Ni showed a decreased peak at 852.6 eV, which could be ascribed to metallic Ni, and an increased peak at 856.0 eV, attributed to oxidized Ni species (Fig. 3f). Therefore, the real catalytically active sites for alcohol oxidation are most likely high-valent nickel species.[39]

In addition to alcohols,[14–18] ammonia[19–21] and urea[22–25] were also explored for the integration with the HER. For instance, Qiao's group recently reported that small-sized MnO_2 ultrathin nanocrystals could act as efficient electrocatalysts for urea oxidation with excellent performance. The catalytic current densities achieved by their MnO_2 electrocatalysts were even greater than that of Pt/C. The same group also explored the oxidation of urea catalyzed by a two-dimensional Ni-based metal organic framework (MOF), which led to a potential reduction of 280 mV compared to that of Pt/C to achieve 10 mA cm^{-2}.[23]

The aforementioned electrocatalysis integrates H_2 production with different organic oxidation reactions, resulting in a potential saving of 200–300 mV relative to that of overall water splitting. However, a cell voltage of approximately 1.3 V is still needed to reach a meaningful current density like 10 mA cm^{-2}. It is highly desirable to explore other organic substrates to further reduce the voltage input for H_2 generation. Along this line, Sun and co-workers chose hydrazine oxidation as the counter reaction to couple the HER using the Ni_2P electrocatalyst coated on nickel foam (Ni_2P/NF).[26] The standard thermodynamic potential of hydrazine oxidation to N_2 is only −0.33 V.[26] As depicted in Fig. 4a, Ni_2P/NF featured interconnected nanosheet arrays with an open network-like nanostructure. The LSV curves of Ni_2P/NF with increasing hydrazine in 1.0 M KOH are compiled in Fig. 4b. In the absence of hydrazine, no oxidation current was observed within the potential window of −0.1 to 0.1 V *vs.* RHE. In contrast, the addition of 0.1 M hydrazine introduced a sharp current increase and increasing the hydrazine concentration from 0.1 to 0.5 M resulted in a rapid increase in oxidation current density, indicative of hydrazine oxidation catalyzed by Ni_2P/NF. As Ni_2P has been reported with high activity towards the HER, Ni_2P/NF could function as a bifunctional electrocatalyst for H_2 production coupled with hydrazine oxidation. Consequently, an electrolyzer using Ni_2P/NF as both an anode and a cathode was then constructed. The Ni_2P/NF couple showed superior performance with a cell voltage of 1.0 V to afford 500 mA cm^{-2} in 1.0 M KOH containing 0.5 M hydrazine (Fig. 4c). In the absence of hydrazine, a cell voltage of 1.6 V was required to reach 20 mA cm^{-2} (Fig. 4d). A 10 h chronopotentiometry experiment revealed a relatively constant cell voltage requirement (0.45 V) to deliver 100 mA cm^{-2}

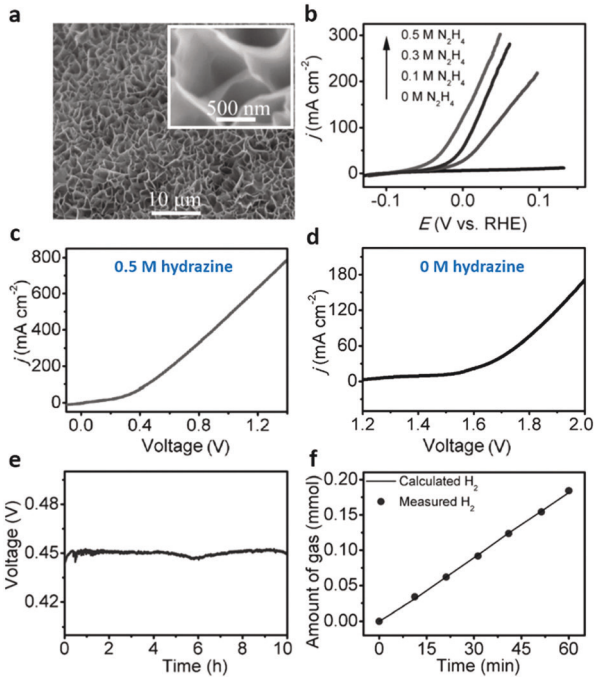

Fig. 4 (a) SEM images of Ni_2P/NF. (b) LSV curves of hydrazine oxidation on Ni_2P/NF in 1.0 M KOH at 5 mV s^{-1}. LSV curves of Ni_2P/NF couple-based electrolysis in 1.0 M KOH at 5 mV s^{-1} with a two-electrode configuration in the presence (c) and absence (d) of 0.5 M hydrazine. (e) Chronopotentiometric curve using a Ni_2P/NF catalyst couple to achieve a current density of 100 mA cm^{-2} in 1.0 M KOH with 0.5 M hydrazine. (f) Gas chromatography-quantified and theoretically calculated H_2 amounts over electrolysis time. Reproduced from ref. 26 with permission from John Wiley and Sons, copyright 2017.

on Ni_2P/NF (Fig. 4e) together with nearly unity Faradaic efficiency (Fig. 4f). Collectively, these results demonstrate that replacing the OER with hydrazine oxidation represents an effective way for efficient H_2 production with a low voltage input.

Although the required voltage for such integrated electrolysis is dramatically reduced relative to that of conventional water electrolysis, the added organic substrates are consumed and transformed to low-value or even harmful by-products. For instance, urea oxidation produces N_2 and CO_2[22] and the oxidation of hydrazine converts the high-energy hydrazine fuel to N_2.[40] Another problem that should not be overlooked is that these gaseous products may mix with the H_2 gas. Therefore, it is even more appealing to explore other organic oxidation reactions which can not only replace the OER but also generate value-added and nongaseous products at the anode.

It is well-known that oxidative biomass upgrading holds a crucial role in converting biomass-derived feedstocks to many value-added chemicals.[29–34,41] Those oxygenated compounds can serve as primary building blocks to produce diverse commodities, polymers, and pharmaceuticals. Among many biomass-derived intermediates, 5-hydroxymethyl furfural (HMF) has been considered as one of the top biomass-derived platform chemicals. For example, one of its oxidation products, 2,5-furandicarboxylic acid (FDCA, Fig. 5a), is an important monomer to produce polyamides, polyesters, and polyurethanes, being a replacement of terephthalic acid.[29,42] Traditional approaches of biomass oxidation often involve stoichiometric chemical oxidants, high temperature, and/or expensive catalysts. However, due to the increasing environmental regulations and economic concerns, efforts have been devoted towards developing ''green'' catalytic processes, wherein catalysts only consist of earth-abundant elements while still exhibiting high activity and robust stability under ambient conditions. In this regard, electrocatalytic oxidation offers an attractive strategy as it is only driven by electricity under ambient conditions and no chemical oxidants are necessary.

We recently reported 3D Ni_2P nanoparticle arrays on Ni foam (Ni_2P NPA/NF) as a bifunctional electrocatalyst to couple H_2 production with HMF oxidation in alkaline media.[29] As revealed by the XRD and SEM measurements, 3D Ni_2P NPA/NF was successfully obtained (Fig. 5b and c). Similar to reported transition metal-based electrocatalysts for the OER and alcohol oxidation,[33,43] an electrochemical activation phenomenon was also observed for Ni_2P NPA/NF during HMF oxidation; hence all the LSV curves in Fig. 5d were collected after the cessation of activation. In the presence of HMF, Ni_2P NPA/NF exhibited an onset potential of 1.35 V *vs.* RHE followed by a rapid current density increase within 1.40 V *vs.* RHE. On the other hand, without HMF, the catalytic onset potential was shifted to 1.5 V *vs.* RHE and no appreciable current could be observed within 1.40 V *vs.* RHE, indicative of more favourable HMF oxidation than the OER on Ni_2P NPA/NF (Fig. 5d). A chronoamperometry experiment was then carried out at 1.423 V *vs.* RHE and the concentration evolutions of HMF and its oxidation products were monitored *via* HPLC measurements (Fig. 5e). Assuming a 100% Faradaic efficiency for the six-electron process of HMF oxidation to FDCA, 59 C was required to consume all the starting HMF. Indeed, as shown in Fig. 5e, after passing the theoretically calculated amount of charge, HMF nearly disappeared and the concentration of FDCA reached the maximum, confirming a nearly unity Faradaic efficiency for both HMF conversion and FDCA production. Even if an anion-exchange membrane was adopted, there still exists a possibility that HMF might migrate to the cathode chamber and hence interfere with the HER on the cathode. Therefore, an ideal HER electrocatalyst should show great selectivity towards H_2 production in the presence of HMF. As an extreme case shown in Fig. 5f, the LSV curves of the HER on Ni_2P NPA/NF in the presence and absence of 10 mM HMF nearly overlapped, indicative of the negligible influence of HMF on H_2 generation catalyzed by Ni_2P NPA/NF.

After establishing the favourable HMF oxidation over the OER and high selectivity of the HER on Ni_2P NPA/NF in the same electrolyte (1.0 M KOH with 10 mM HMF) with the three-electrode configuration, we next assembled a two-electrode electrolyzer for the integrated HER and HMF oxidation using Ni_2P NPA/NF as both an anode and a cathode. After introducing 10 mM HMF into the electrolyte (1.0 M KOH), the onset cell voltage was dramatically reduced (Fig. 5g). Fig. 5h presents that nearly 200 mV voltage input was saved to reach benchmark current densities like 10, 20, and 50 mA cm^{-2}, highlighting the much better energy conversion efficiency of the integrated HER and HMF oxidation relative to water splitting alone. Gas chromatography measurements further confirmed a nearly 100% Faradaic efficiency for H_2 production (Fig. 5i) and no O_2 was detected during the electrolysis at 1.50 V. Quantifying the resulting electrolyte by HPLC also resulted in a high Faradaic efficiency of $\sim$97% for FDCA production. Such excellent Faradaic efficiencies for both the HER and FDCA generation could be maintained for at least three consecutive electrolysis cycles employing the same Ni_2P NPA/NF electrocatalyst couple (Fig. 5j). Collectively, these combined results undoubtedly proved the success of our proposed integrated electrolysis producing two valuable products (H_2 and FDCA) with a lower energy input.

Encouraged by the above results, we further explored the electrocatalytic upgrading of various biomass-derived compounds like furfural and furfuryl alcohol on other nonprecious bifunctional electrocatalysts.[30] The high overpotential requirement of the OER actually grants us a large potential window to perform various organic oxidation reactions catalyzed by low-cost electrocatalysts. For instance, Ni_3S_2 could be adopted as a model electrocatalyst, which was prepared by straightforward sulfurization of commercially available nickel foams (Ni_3S_2/NF). Low-magnification SEM images of Ni_3S_2/NF indicated an interconnected macroporous 3D framework (Fig. 6a), similar to that of pristine Ni foam. Different from the featureless morphology of Ni foam, highly-magnified SEM images of Ni_3S_2/NF revealed an interesting structure composed of stacked nanoparticles (Fig. 6b and c). A close inspection of these nanoparticles in a high-resolution SEM image revealed the presence of abundant mesopores on the surface of Ni_3S_2/NF (Fig. 6b). Such a unique hierarchically porous nanostructure was expected to boost the

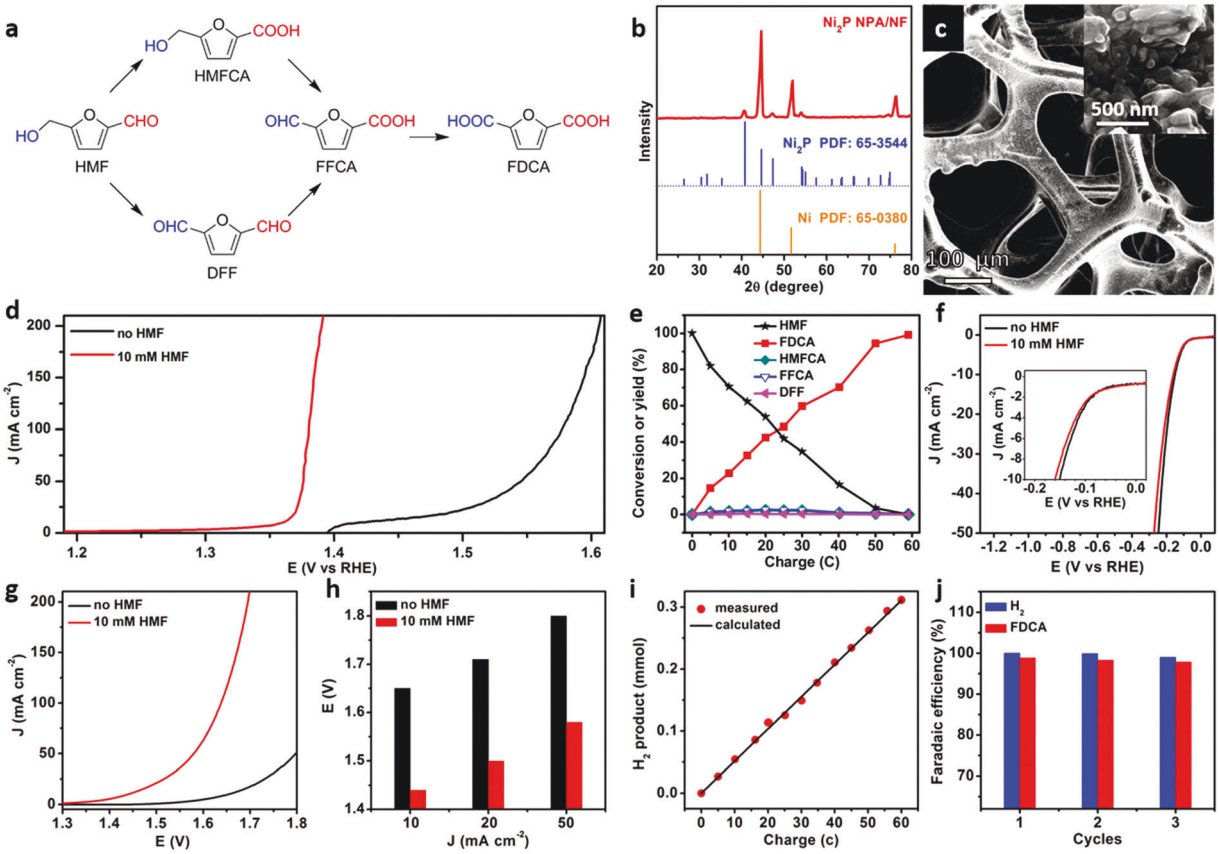

Fig. 5 (a) Two possible pathways of HMF oxidation to FDCA. (b) XRD pattern and (c) SEM images of Ni_2P NPA/NF. (d) LSV curves of Ni_2P NPA/NF at 2 mV s^{-1} in 1.0 M KOH with and without 10 mM HMF. (e) Conversion and yield changes of HMF and its oxidation products during the electrochemical oxidation of HMF at 1.423 V *vs.* RHE in 1.0 M KOH with 10 mM HMF. (f) LSV curves of Ni_2P NPA/NF at 2 mV s^{-1} in 1.0 M KOH with and without 10 mM HMF. (g) LSV curves and (h) comparison of the cell voltages to achieve benchmark current densities for a Ni_2P NPA/NF catalyst couple in 1.0 M KOH with and without 10 mM HMF. (i) GC-measured H_2 quantity compared with the theoretically calculated amount assuming a 100% Faradaic efficiency. (j) Faradaic efficiencies of the Ni_2P NPA/NF catalyst couple for simultaneous H_2 and FDCA generation in 1.0 M KOH solution with 10 mM HMF for three successive electrolysis cycles. Reproduced from ref. 29 with permission from John Wiley and Sons, copyright 2016.

accessibility of catalytically active sites and facilitate mass transport, beneficial to electrocatalytic performance.[38] Elemental mapping analysis of Ni_3S_2/NF confirmed the uniform distribution of Ni and S (Fig. 6d–f), validating the chemical conversion of Ni into Ni_3S_2. Five representative organic oxidation reactions were catalyzed by Ni_3S_2/NF in parallel. As compiled in Fig. 6g–k, all the LSV curves in the presence of organic substrates universally took off at much lower potentials compared to those in the absence of organics, consistent with their more favourable oxidation relative to water oxidation. Interestingly, all the catalytic currents of organic oxidation rose at very similar potentials (~1.36 V *vs.* RHE), regardless of which the organic substrate was oxidized. This phenomenon evokes a reminiscence of the oxidation of various benzyl alcohol derivatives catalyzed by hp-Ni (Fig. 3e). A two-electrode electrolyzer employing Ni_3S_2/NF as both the cathode and anode required a much lower voltage input for H_2 production coupled with HMF oxidation to achieve benchmark current densities (10, 20, 50, and 100 mA cm^{-2}) relative to pure water splitting electrolysis using the same electrode couple (Fig. 6l). For example, in order to produce a current density of 100 mA cm^{-2}, a voltage of 1.64 V was needed for the integrated electrolysis; while for overall water splitting electrolysis, 1.84 V was required to arrive at the same current density. Although the low-magnified SEM image (Fig. 6m) of post-HMF Ni_3S_2/NF indicated the maintenance of the overall 3D hierarchically porous configuration and primary Ni_3S_2 phase, high-magnification SEM images (Fig. 6n and o) revealed the presence of featureless monoliths, different from the pristine sample (Fig. 6b and c). The elemental mapping images in Fig. 6p indicate that the post-HMF oxidation Ni_3S_2/NF mainly consisted of Ni and S, plus a large concentration of O_2 over the newly formed monoliths, indicating the oxidation of Ni_3S_2 during electrolysis. In addition to these aforementioned examples, many other electrocatalytic systems have been explored for the coupled H_2 evolution and organic oxidation, which are summarized in Table 1.

3. Photocatalytic HER integrated with organic oxidation

Besides electrocatalytic H_2 production from water with electricity as the energy input, photocatalysis provides another more

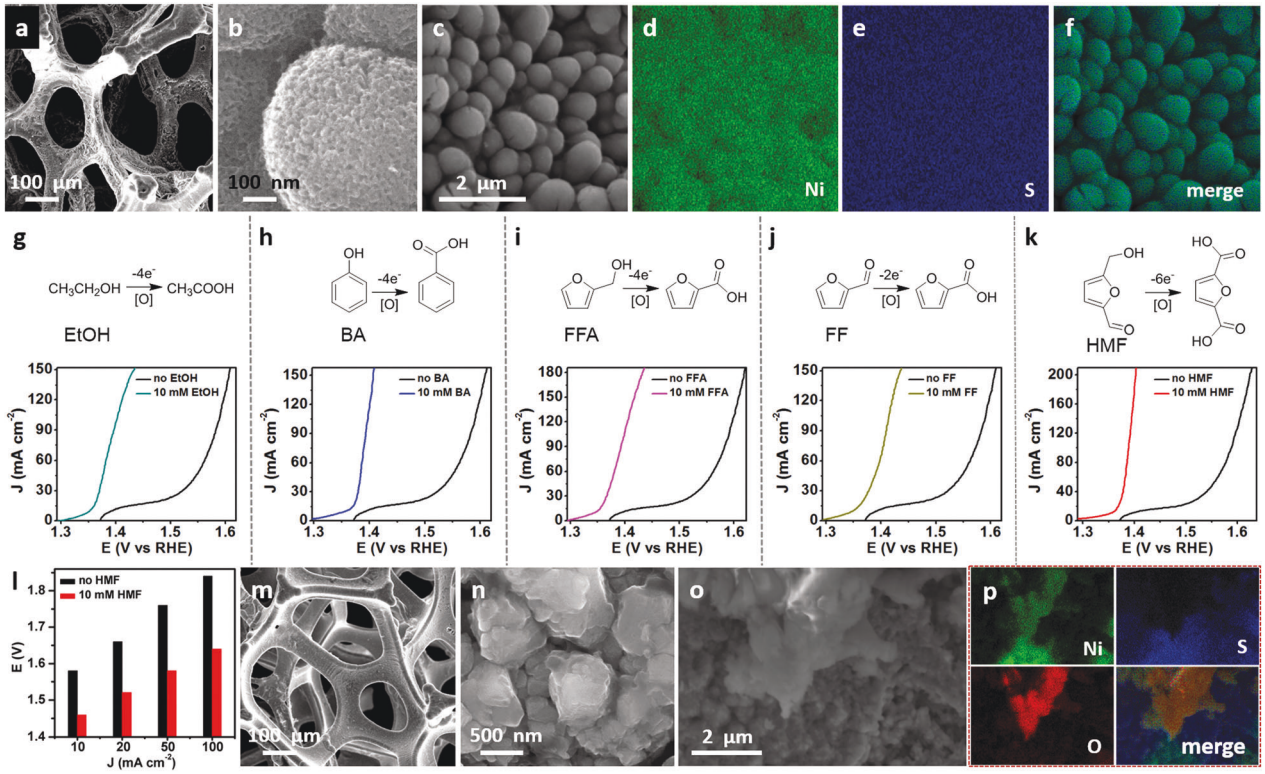

Fig. 6 (a–c) SEM images at different magnifications and (d–f) elemental mapping images of Ni_3S_2/NF. (g–k) LSV curves of selected organics (10 mM) to value-added products compared to water oxidation catalyzed by Ni_3S_2/NF at 2 mV s^{-1} in 1.0 M KOH (EtOH: ethanol; BA: benzyl alcohol; FFA: furfuryl alcohol; FF: furfural; HMF: 5-hydroxymethylfurfural). (l) Comparison of the cell voltages to achieve benchmark current densities for a Ni_3S_2/NF catalyst couple in 1.0 M KOH with and without 10 mM HMF. (m–p) SEM images at different magnifications and elemental mapping images of Ni_3S_2/NF after HMF oxidation. Reproduced from ref. 30 with permission from American Chemical Society, copyright 2016.

direct approach to convert and store solar energy in chemical bonds.[44–46] In fact, light-driven water splitting for H_2 evolution has attracted much research interest during the last few decades. Since the discovery of photoelectrochemical water splitting on TiO_2 in 1972,[47] extensive studies have been conducted for photo-driven H_2 evolution on semiconductors.[48] Generally, three steps are involved in semiconductor-based photocatalysis: (i) light absorption and photogeneration of electron–hole pairs, (ii) migration of photogenerated electron–hole pairs to the respective sites, and (iii) charge utilization for H_2 production and another oxidation reaction. An ideal semiconductor should meet at least two criteria: a suitable band gap for efficient light absorption and appropriate band positions for sufficient reducing and oxidizing power.

In order to minimize the recombination of excited electrons and holes upon light irradiation, sacrificial electron donors are usually employed in photocatalytic systems for H_2 production. However, such a conventional strategy not only increases the overall cost of H_2 production, but also wastes the oxidizing power of excited holes. Analogous to the scenario successfully demonstrated for the integrated HER and organic oxidation in the aforementioned electrocatalytic systems, it is quite appealing to seek alternative organic oxidation reactions to consume the photogenerated holes on semiconductors while simultaneously producing value-added organic products. Recent years have witnessed the emergence of such an integrated photocatalysis strategy for the HER and organic reforming on several semiconductor systems, including carbon nitride and cadmium chalcogenides. Among various organic oxidation reactions, the photo-driven oxidation of alcohols to aldehydes shows great promise to be coupled with H_2 generation.[49–51]

3.1 Carbon nitride-based photocatalysts

Carbon nitride (CN_x) has emerged as a great semiconductor in recent years because of its visible light absorption and well-positioned valence and conduction bands for many important redox reactions, including water splitting.[52] For instance, Sun *et al.* reported a hybrid photocatalyst system, utilizing C_3N_4 as the semiconductor, and a ruthenium complex and platinum as the oxidation and reduction catalysts, respectively, for the photo-induced benzyl alcohol oxidation and H_2 evolution.[53] The presence of the molecular ruthenium catalyst remarkably improved the selectivity of benzyl alcohol oxidation to benzyl-aldehyde primarily due to the formation of Ru(IV)═O active species. Similarly, Yang and his co-workers synthesized fibrous Ag nanoparticles decorated on g-C_3N_4 aerogel.[54] This photocatalytic system exhibited excellent photocatalytic performance for H_2 evolution in the presence of methanol, which was oxidized to formaldehyde. Nevertheless, the utilization of expensive metals (Pt, Ru, and Ag) in these photocatalytic systems inevitably

Table 1 Representative electrocatalytic hydrogen evolution coupled with organic oxidation in aqueous media

Catalyst	Electrolyte	Organic substrate	Organic product	Three-electrode setup			Two-electrode setup		FE (%)		Ref.
				η_{HER} (V)	η_{OER} (V)	$\eta_{organic}$ [a]	V_1 [b] (V)	V_2 [c] (V)	HER	Org.	
Pd/TNTA-web	2.0 M NaOH	2 M Ethanol	Acetic acid	—	—	—	1.76 (1000)	0.69	—	—	14
F-β-FeOOH	1.0 M KOH	Ethanol : H_2O = 15 : 5	Acetic acid	—	1.59	1.207	1.51	1.43	91.7	~72	15
Ni_2S/CFC	1.0 M KOH	0.45 M 2-Propanol	Acetone	−0.21	1.515	1.348	—	—	100	98	16
NC@$CuCo_2N_x$/CF	1.0 M KOH	15 mM Benzyl alcohol	Benzaldehyde	−0.105	1.46	1.25	1.62	1.55	97.4	~81	17
Co_3O_4 NSs/CP	1.0 M KOH	1 M Ethanol	Ethyl acetate	—	1.50	1.445	—	—	—	98	18*a*
3D PdCu alloy	1.0 M KOH	1 M Ethanol	Ethyl acetate	−0.106	—	1.56 (onset)	—	—	—	—	18*b*
S-MnO_2/NF	1.0 M KOH	0.5 M Urea	None	—	—	1.33	—	1.41	—	—	22
Ni_2P/NF	1.0 M KOH	0.5 M Hydrazine	None	−0.29 (200)	—	0.018 (200)	1.6 (20)	1.0 (500)	100	—	26
CoP/TiM	1.0 M KOH	0.1 M Hydrazine	None	—	1.55 (onset)	−0.05 (onset)	1.65	0.2	100	—	27
Cu_3P/CF	1.0 M KOH	0.5 M Hydrazine	None	−0.496 (100)	—	0.152 (100)	1.85	0.72 (100)	—	—	28
Ni_2P NPA/NF	1.0 M KOH	10 mM HMF	FDCA	−0.15	1.50 (onset)	1.35 (onset)	1.65	1.44	100	98	29
Ni_3S_2/NF	1.0 M KOH	10 mM HMF	FDCA	−0.16	1.50 (onset)	1.35 (onset)	1.58	1.46	100	98	30
Co–P/CF	1.0 M KOH	50 mM HMF	FDCA	—	1.53 (20)	1.38 (20)	1.59 (20)	1.44 (20)	100	—	31
Ni_2P/Ni/NF	1.0 M KOH	30 mM Furfural	Furoic acid	—	1.55 (onset)	1.43 (onset)	1.59	1.48	100	100	32
hp-Ni	1.0 M KOH	10 mM Benzyl alcohol	Benzoic acid	−0.219 (50)	1.51 (onset)	1.35 (onset)	1.69	1.50	100	97	33
Fe–CoP/CC	1.0 M KOH	5 mL of Aloe extract	—	−0.359 (100)	1.707 (25)	1.572 (25)	1.57	1.44	100	—	34*a*
CoP NWs/CC	1.0 M KOH	40 mg L^{-1} Triclosan	Phenol	−0.069	1.59	1.54	1.68	1.63	100	—	35
Fe_2P/SSM	10 M KOH	0.5 M Glucose	—	—	1.43 (onset)	1.33 (onset)	1.52	1.22	100	—	36
Nano-Cu foam	0.1 M KOH	5 mM HMF	FDCA	—	1.6 (onset)	1.25 (onset)	—	—	100	95.3	42*b*

[a] All the potentials are reported as V *vs.* RHE. If not indicated, the listed potentials are those to achieve 10 mA cm^{-2}. Numbers in parentheses are current densities in mA cm^{-2}. [b] V_1 is the cell voltage for pure water splitting. [c] V_2 is the cell voltage for the integrated HER with organic oxidation.

results in high cost for large-scale applications. It is more desirable to explore non-precious alternatives.

In 2016, Reisner *et al.* reported a hybrid photocatalytic system consisting of carbon nitride decorated with cyanamide on the surface and a molecular nickel(II) bis(diphosphine) catalyst to integrate light-driven H_2 evolution and benzylic alcohol oxidation (Fig. 7).[55] Under optimized conditions, such a hybrid system showed a high activity towards the HER and aldehyde production with a rate of 763 μmol g^{-1} h^{-1} and a quantum efficiency of 15%. A turnover frequency of 76 h^{-1} was calculated based on the amount of nickel and the conversion of 4-methylbenzyl alcohol reached 83.0%. Transient absorption spectroscopy studies demonstrated that the presence of cyanamide groups on the surface of carbon nitride was critical in that these groups would suppress the recombination of excited electrons and holes, leading to a higher production yield. Unfortunately, this hybrid system had a relatively short operational lifetime, most likely due to the poor stability of the nickel catalyst under photocatalysis conditions.

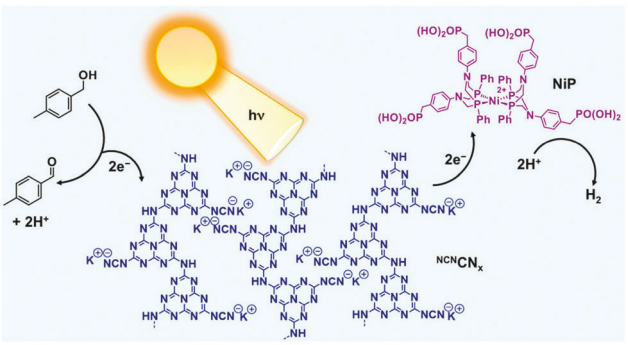

Fig. 7 Schematic representation of a closed redox system for solar-driven H_2 evolution coupled with alcohol oxidation in aqueous media. Reproduced from ref. 55 with permission from American Chemical Society, copyright 2016.

3.2 Cadmium chalcogenide-based photocatalysts

Another popular semiconductor candidate for photocatalysis applications is CdS whose conduction band lies at −0.5 V *vs.* NHE and valence band at +1.9 V *vs.* NHE.[56–60] Feldmann's group reported an interesting CdS-based photocatalytic system utilizing a low-cost nickel co-catalyst for H_2 production integrated with alcohol oxidation.[58] A unique redox shuttle mechanism was proposed. Under light irradiation, hydroxyl anions diffuse to the surfaces of the CdS nanorods and are oxidized to hydroxyl radicals by excited holes. The *in situ* formed hydroxyl radicals later oxidize ethanol to acetaldehyde (Fig. 8a). Nickel nanoparticles were expected to catalyze H_2 evolution. The size

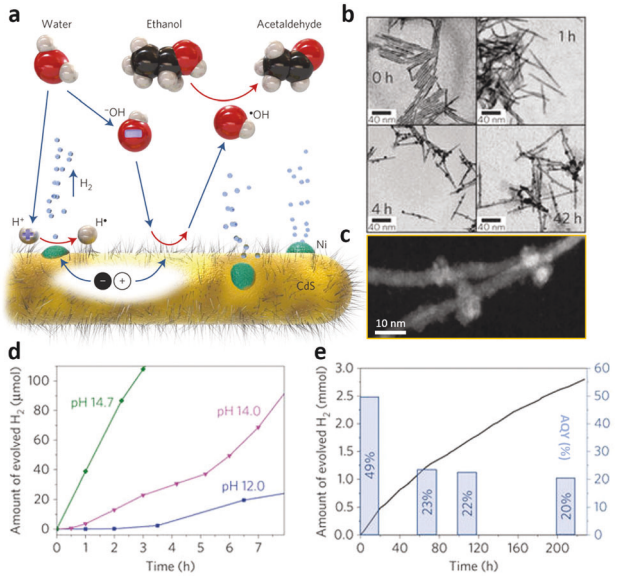

Fig. 8 (a) Schematic of photocatalytic H_2 generation following a redox shuttle mechanism. (b) TEM images of CdS nanorods after photodeposition of nickel as a function of illumination time. (c) HAADF-STEM image of CdS decorated with nickel nanoparticles. (d) Amount of evolved H_2 *vs.* time at different pHs. (e) Long-term H_2 evolution *vs.* illumination time with 10% ethanol. The bars denote the apparent quantum yields (AQYs) at 447 nm averaged over 20 h of illumination. Reproduced from ref. 58 with permission from Springer Nature, copyright 2014.

and quantity of nickel nanoparticles on CdS could be conveniently controlled by photodeposition (Fig. 8b and c). The authors also investigated the pH influence on H_2 production. As shown in Fig. 8d, the amount of evolved H_2 was substantially larger at higher pH, probably due to fast alcohol oxidation with increasing alkalinity. The apparent quantum yield for H_2 production was measured as high as 49% over the first 20 h under irradiation with a light wavelength of 447 nm. Longer photolysis resulted in a lower quantum yield (~20%). Overall, such a hybrid photocatalytic system exhibited great stability, showing decent activity up to at least 220 h (Fig. 8e).

In order to increase the specific surface area and maximize the utilization of excited electrons and holes for photocatalysis applications, an ultrathin two-dimensional (2D) nanosheet is a preferred morphology for semiconductors.[61,62] Last year, our group developed a microwave synthesis to prepare ultrathin 2D CdS nanosheets. With the assistance of the nickel co-catalyst, our Ni/CdS photocatalyst was able to drive H_2 evolution and organic upgrading under visible light irradiation.[63] After microwave treatment, the wurtzite crystal structure of CdS was obtained and no crystalline peaks due to nickel could be observed for Ni/CdS (Fig. 9a). The ultrathin thickness of Ni/CdS was measured at ~1.1 nm based on the atomic force microscopy (AFM) results in Fig. 9b. In contrast to previous studies where benzyl alcohol or ethanol was chosen as the organic substrate, our group was more interested in exploring the photocatalytic upgrading of biomass-derived intermediate compounds coupled with H_2 evolution. In particular, we sought to conduct photo-induced valorization of furfural alcohol and HMF to furfural and 2,5-diformylfuran (DFF) in neutral water, respectively. As shown in Fig. 9c, under visible light irradiation, our 2D Ni/CdS nanosheets exhibited excellent performance for H_2 evolution when furfural alcohol was used as the organic substrate. In the meantime, furfural alcohol was converted to furfural with a nearly 100% yield within 22 h of irradiation (Fig. 9d). Surprisingly, when HMF was adopted as the organic substrate, a much lower H_2 production rate was observed and it was not able to completely oxidize HMF to DFF after 22 h of photolysis (yield ~22%), even though a similar oxidation from an alcohol group to an

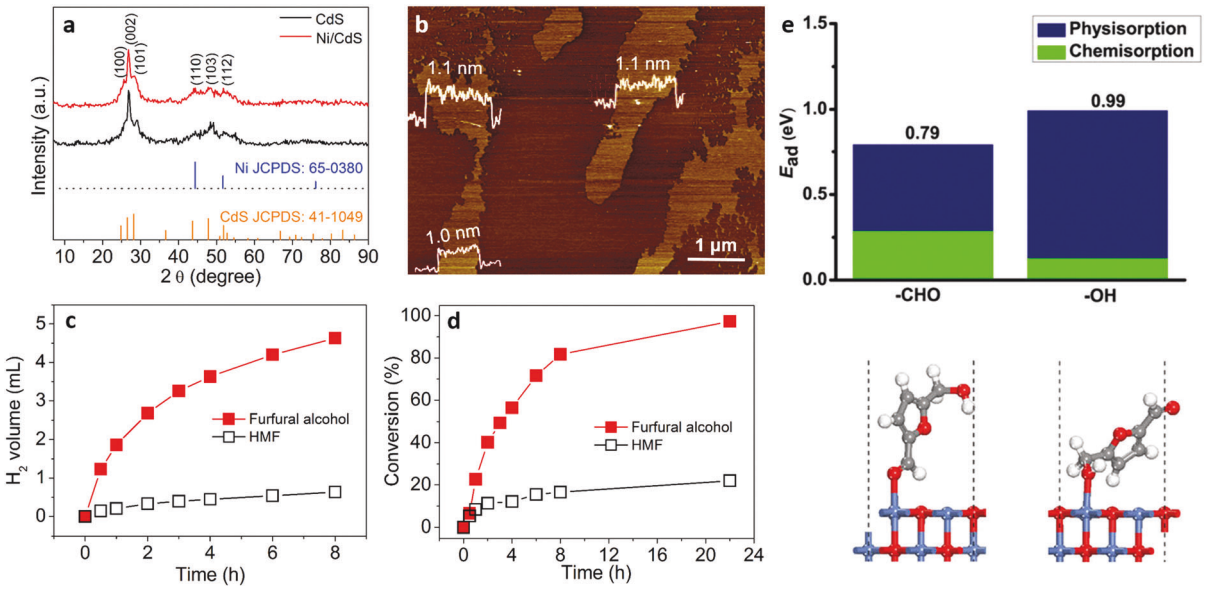

Fig. 9 (a) XRD pattern and (b) AFM image of Ni/CdS. (c) Produced H_2 and (d) conversion of organic substrates during photocatalysis. (e) Adsorption structures and energies of HMF at the water/NiO(001) interface *via* its aldehyde or alcohol group. Reproduced from ref. 63 with permission from American Chemical Society, copyright 2017.

aldehyde group took place in both cases. The remarkable difference was further investigated *via* theoretical computations (Fig. 9e). It was rationalized that the binding affinity of the aldehyde group in HMF towards nickel oxide was slightly stronger than its alcohol group; therefore, the aldehyde group more likely adsorbed on Ni/CdS, while the alcohol group was kept away from the oxidizing sites, resulting in a slower oxidation of HMF to DFF. However, under alkaline conditions, both furfural alcohol and HMF were oxidized to their corresponding carboxylates with yields over 90%.

Given the great abundance of biomass as a sustainable and renewable carbon source, it remains a hot topic in exploring the direct conversion of biomass materials to value-added products, not only focusing on those biomass-derived small molecular intermediates but also cracking the stubborn polymeric components. As lignocellulose is one of the most prevalent biomass materials, increasing research efforts have been centered on its upgrading and utilization *via* green methods. Complex polymeric structures are involved in all three main components of lignocellulose including cellulose, hemicellulose and lignin (Fig. 10a). Conventional biomass reforming processes usually require high temperature and expensive chemicals, which may result in carbon-based gaseous products like CO, CO_2, and CH_4. In contrast, visible light-driven reformation of lignocellulose to produce H_2 represents an alternative green approach. Last year, Reisner's group reported an interesting strategy for photo-induced H_2 production using lignocellulose and even raw biomass materials (Fig. 10b) as the hole scavengers to boost H_2 evolution,

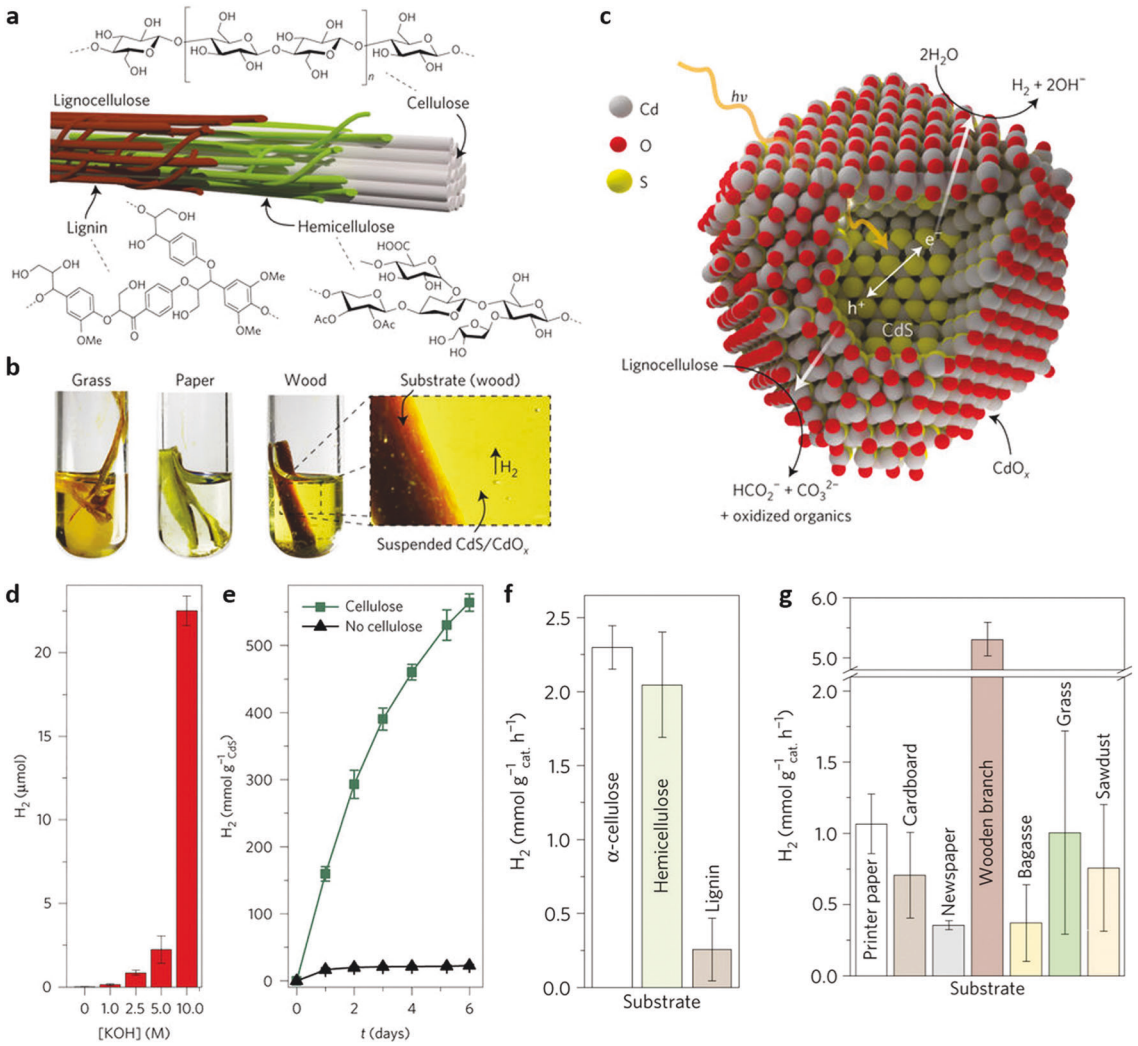

Fig. 10 (a) Lignocellulose exists as microfibrils in plant cell walls and is composed of cellulose surrounded by hemicellulose and lignin. (b) These components can be photo-reformed into H_2 using CdS coated with CdO_x. (c) This combination creates a highly robust photocatalyst capable of producing H_2 from lignocellulose when suspended in alkaline solution and irradiated with sunlight. (d) The pH dependence of the photocatalytic H_2 evolution from a 2 mL aqueous solution of ligand-free CdS (0.5 μM) with 50 mg mL^{-1} α-cellulose after 18 h of irradiation. (e) Long-term photocatalytic cumulative production of H_2 by CdS (0.5 μM) with and without 50 mg mL^{-1} α-cellulose in 2 mL of KOH (10.0 M). Photocatalytic production of H_2 (AM 1.5G, 100 mW cm^{-2}) over 24 h with CdS (0.5 μM) and $Co(BF_4)_2$ (0.34 mM) in 2 mL of KOH (10.0 M, 25 °C, anaerobic atmosphere) with (f) 50 mg mL^{-1} α-cellulose, 25 mg mL^{-1} hemicellulose and 0.25 mg mL^{-1} lignin and (g) 50 mg mL^{-1} raw and waste biomass substrates. Reproduced from ref. 60 Springer Nature, copyright 2017.

Table 2 Representative photocatalytic hydrogen evolution coupled with organic oxidation

Catalyst	Light source	Time (h)	Solvent	Substrate	Product	H_2 (μmol)	Conv. (%)	Sel. (%)	Ref.
Pt/TiO_2	UV	1	CH_3CN	Benzyl alcohol	Benzaldehyde	48	99	>99	50*e*
$Pd/CdS–TiO_2$	Blue LED (460 nm, 10 mW cm^{-2})	4	H_2O	Benzyl alcohol	Benzaldehyde	36	96	>99	51*b*
$Pt–g\text{-}C_3N_4$	300 W Xe lamp (λ > 400 nm)	20	H_2O	Benzyl alcohol	Benzaldehyde	51	40	90	53
$^{NCN}CN_x–NiP$	1 sun irradiation	24	0.02 M KP_i	4-Methyl-benzyl alcohol	4-Methyl-benzaldehyde	21.3	66.0	100	55
CdS/CdO_x	Solar light (100 mW cm^{-2})	24	10 M KOH	Paper	—	12.37	—	—	56*a*
		144		α-Cellulose	—	18.42	9.21	—	
Co/CdS	300 W Xe lamp (λ > 420 nm)	3	CH_3CN	Benzyl alcohol	Benzaldehyde	202.0	18.5	94.4	59*b*
Ni/CdS	8 W blue LED (λ = 450 nm)	8	H_2O	Furfural alcohol	Furfural	160.5	81.7	100	63
$CdSe–Ni^{2+}$	Purple LED (λ = 410 nm)	6	H_2O	Fenzyl alcohol	Benzaldehyde	87	92	98	65
$Ru/SrTiO_3$:Rh	300 W Xe lamp (λ > 420 nm)	24	Toluene/H_3PO_4	(4-Methoxyphenyl)-methanol	4-Methoxy benzaldehyde	247.5	92	100	67

in which CdS quantum dots were utilized as the semiconductors.[60] Because of the quantum confinement effect, high specific surface area, and tunable band gap based on size, quantum dots have enormous potential for photocatalysis.[64] In order to overcome the photo-corrosion of CdS quantum dots and simultaneously increase the solubility of biomass substrates, a highly alkaline electrolyte was applied, which was able to promote the formation of a cadmium oxide (CdO_x) layer on the surface of CdS (Fig. 10c). It was found that the solution pH had a dramatic impact on H_2 evolution. As shown in Fig. 10d, increasing the alkalinity resulted in higher H_2 production and the best activity was achieved in 10.0 M KOH when α-cellulose was used as the hole scavenger. Control experiments conducted in the absence of cellulose clearly proved the critical role played by cellulose in boosting the H_2 yield, in that the addition of cellulose to the reaction solution dramatically enhanced the H_2 production rate by several magnitudes (Fig. 10e). In addition to α-cellulose, hemicellulose and lignin were also found to increase the H_2 production rate, albeit the performance of lignin was much lower than those of the former two substrates (Fig. 10f). The authors further tested several crude biomass materials, such as printer paper, cardboard, newspaper, wooden branches, grass, and sawdust (Fig. 10g), among which the wooden branches demonstrated the best activity with a H_2 production rate over 5 mmol g_{cat}^{-1} h^{-1}, which was even higher than those obtained from α-cellulose, ~2.3 mmol g_{cat}^{-1} h^{-1} (Fig. 10f). This seminal report highlighted the great promise of directly utilizing raw biomass materials to drive H_2 production with visible light irradiation under ambient conditions. Future efforts should focus on producing valuable chemicals from the oxidation of those raw biomass materials, rather than merely acting as hole scavengers for the HER.

In addition to the aforementioned photocatalytic systems based on CN_x, and CdS, other robust semiconductors like CdSe,[65] Au–Pd/ZrO_2,[66] $Ru/SrTiO_3$:Rh,[67] and MgO[68] have also been applied in H_2 photogeneration coupled with organic oxidation reactions. For instance, Wu's group applied 3-mercaptopropionic-capped CdSe quantum dots to accomplish alcohol oxidation integrated with H_2 generation.[65] A cascade catalytic cycle involving the generation of thiol radicals was proposed for their photocatalytic system. The *in situ* generated thiol radicals might be utilized for other complex organic reactions. A list of representative photocatalytic systems for the coupled H_2 evolution and organic oxidation is included in Table 2.

4. Conclusions

In this Feature Article, we have summarized the recent progress in electrocatalytic and photocatalytic water splitting integrated with organic oxidation for efficient H_2 generation and organic transformation. Such a new catalysis strategy is complementary to conventional focus on catalyst design in minimizing the overpotential requirements for both the HER and OER in pure water splitting. Instead, it suggests that thermodynamically more favourable organic oxidation reactions be adopted to replace the OER, as they have several intrinsic advantages, such as eliminating the formation of explosive H_2/O_2 mixtures and reactive oxygen species (ROS), improving the efficiency of H_2 production and potential co-production of value-added organic products. Even though such a novel direction in electro- and photocatalysis is still in an early stage, quite a few organic substrates have been explored, including alcohols, ammonia, urea, hydrazine, biomass-derived platform chemicals and even raw biomass materials.

In the electrocatalysis field, earth-abundant materials like first-row transition metals have found promising applications as electrocatalysts for both the HER and the accompanying organic oxidation reactions. However, the overpotential requirements for those organic oxidation reactions are still quite high. Given the much lower thermodynamic potentials of those organics relative to that of the OER, much smaller oxidation potentials should be realized to drive their oxidation. In addition, electrocatalytic selectivity towards the most desirable products should be further improved. In some cases, the poison issue of electrocatalysts by organic substrates could be severe. It is thus a long-term challenge to explore highly efficient, robust, and selective electrocatalysts with low-cost for this coupling electrocatalysis strategy. In order to achieve sufficient conductivity, an electrolyte (*i.e.*, KOH) with high concentration is typically required. Therefore, the separation and purification of the obtained organic products from aqueous electrolytes at low cost should also be considered.

In the photocatalysis field, it is exciting to see raw biomass materials that could be directly utilized as hole scavengers for

photo-induced H_2 production. Nevertheless, the scope of explored semiconductors is still limited and most of them do not absorb a large portion of the solar spectrum. Considering the lower oxidizing power requirement of many organic reactions relative to that of water oxidation, it is anticipated that a much larger pool of semiconductors can be considered as candidates for this coupling photocatalysis strategy in the future. Currently, only relatively simple organic oxidation reactions (*i.e.*, alcohol oxidation) have been integrated with H_2 evolution in both electrocatalysis and photocatalysis. In order to enlarge the versatility and demonstrate the real potential of this coupling catalysis approach, it is highly desirable to explore more challenging yet useful organic reactions, such as oxidative C–C coupling. One could even envisage coupling both organic reactions to complete the redox cycle of electro- and photocatalysis. In addition, developing efficient and robust membranes to separate the organics should also be taken into account. Overall, with the development of competent catalysts and semiconductors, more exciting results in this burgeoning field of integrating reduction and oxidation reactions in both electrolyzers and photo-reactors can be certainly expected.

Conflicts of interest

There are no conflicts to declare.

Acknowledgements

We acknowledge the financial support of Utah State University and the National Science Foundation (CAREER CHE-1653978).

Notes and references

1 (*a*) S. Chu, Y. Cui and N. Liu, *Nat. Mater.*, 2017, **16**, 16; (*b*) N. S. Lewis and D. G. Nocera, *Proc. Natl. Acad. Sci. U. S. A.*, 2006, **103**, 15729; (*c*) B. You and Y. Sun, *Acc. Chem. Res.*, 2018, **51**, DOI: 10.1021/acs.accounts.8b00002.
2 (*a*) B. M. Hunter, H. B. Gray and A. M. Müller, *Chem. Rev.*, 2016, **116**, 14120; (*b*) C. G. Morales-Guio and X. Hu, *Acc. Chem. Res.*, 2014, **47**, 2671.
3 (*a*) Z. W. Seh, J. Kibsgaard, C. F. Dickens, I. Chorkendorff, J. K. Nørskov and T. F. Jaramillo, *Science*, 2017, **355**, 4998; (*b*) B. You and Y. Sun, *ChemPlusChem*, 2016, **81**, 1045.
4 (*a*) S. Chu and A. Majumdar, *Nature*, 2012, **484**, 294; (*b*) H. B. Gray, *Nat. Chem.*, 2009, **1**, 7.
5 (*a*) J. H. Montoya, L. C. Seitz, P. Chakthranont, A. Vojvodic, T. F. Jaramillo and J. K. Nørskov, *Nat. Mater.*, 2017, **16**, 70; (*b*) D. G. Nocera, *Acc. Chem. Res.*, 2012, **45**, 767.
6 (*a*) D. G. Nocera, *Acc. Chem. Res.*, 2017, **50**, 616; (*b*) T. Asefa, *Acc. Chem. Res.*, 2016, **49**, 1873; (*c*) V. R. Stamenkovic, D. Strmcnik, P. P. Lopes and N. M. Markovic, *Nat. Mater.*, 2017, **16**, 57; (*d*) J. Hwang, R. R. Rao, L. Giordano, Y. Katayama, Y. Yu and Y. Shao-Horn, *Science*, 2017, **358**, 751.
7 M. R. Gao, Y. R. Zheng, J. Jiang and S. H. Yu, *Acc. Chem. Res.*, 2017, **50**, 2194.
8 (*a*) D. Kang, T. W. Kim, S. R. Kubota, A. C. Cardiel, H. G. Cha and K.-S. Choi, *Chem. Rev.*, 2015, **115**, 12839; (*b*) K. Chang, X. Hai and J. Ye, *Adv. Energy Mater.*, 2016, **6**, 1502555; (*c*) J. Qi, W. Zhang and R. Cao, *Adv. Energy Mater.*, 2017, **7**, 1701620; (*d*) S. Wang and X. Wang, *Small*, 2015, **11**, 3097.
9 M. Carmo, D. L. Fritz, J. Mergel and D. Stolten, *Int. J. Hydrogen Energy*, 2013, **38**, 4901.
10 J. R. McKone, N. S. Lewis and H. B. Gray, *Chem. Mater.*, 2014, **26**, 407.
11 (*a*) B. Rausch, M. D. Symes, G. Chisholm and L. Cronin, *Science*, 2014, **345**, 1326; (*b*) M. D. Symes and L. Cronin, *Nat. Chem.*, 2013, **5**, 403; (*c*) B. Rausch, M. D. Symes and L. Cronin, *J. Am. Chem. Soc.*, 2013, **135**, 13656.
12 (*a*) L. Chen, X. Dong, Y. Wang and Y. Xia, *Nat. Commun.*, 2016, **7**, 11741; (*b*) A. Landman, H. Dotan, G. E. Shter, M. Wullenkord, A. Houaijia, A. Maljusch, G. S. Grader and A. Rothschild, *Nat. Mater.*, 2017, **16**, 646.
13 W. Li, N. Jiang, B. Hu, X. Liu, F. Song, G. Han, T. J. Jordan, T. B. Hanson, T. L. Liu and Y. Sun, *Chem*, 2018, **4**, 637.
14 Y. X. Chen, A. Lavacchi, H. A. Miller, M. Bevilacqua, J. Filippi, M. Innocenti, A. Marchionni, W. Oberhauser, L. Wang and F. Vizza, *Nat. Commun.*, 2014, **5**, 4036.
15 G. F. Chen, Y. Luo, L. X. Ding and H. Wang, *ACS Catal.*, 2018, **8**, 526.
16 T. Wu, X. Zhu, G. Wang, Y. Zhang, H. Zhang and H. Zhao, *Nano Res.*, 2018, **11**, 1004.
17 J. Zheng, X. Chen, X. Zhong, S. Li, T. Liu, G. Zhuang, X. Li, S. Deng, D. Mei and J. G. Wang, *Adv. Funct. Mater.*, 2017, **27**, 1704169.
18 (*a*) L. Dai, Q. Qin, X. Zhao, C. Xu, C. Hu, S. Mo, Y. O. Wang, S. Lin, Z. Tang and N. Zheng, *ACS Cent. Sci.*, 2016, **2**, 538; (*b*) X. Zhao, L. Dai, Q. Qin, F. Pei, C. Hu and N. Zheng, *Small*, 2017, **13**, 1602970.
19 W. Xu, R. Lan, D. Du, J. Humphreys, M. Walker, Z. Wu, H. Wang and S. Tao, *Appl. Catal., B*, 2017, **218**, 470.
20 J. Gwak, M. Choun and J. Lee, *ChemSusChem*, 2016, **9**, 403.
21 F. Vitse, M. Cooper and G. G. Botte, *J. Power Sources*, 2005, **142**, 18.
22 S. Chen, J. Duan, A. Vasileff and S. Z. Qiao, *Angew. Chem., Int. Ed.*, 2016, **55**, 3804.
23 D. D. Zhu, C. Guo, J. Liu, L. Wang, Y. Du and S. Z. Qiao, *Chem. Commun.*, 2017, **53**, 10906.
24 G. Wang, j. Chen, Y. Li, J. Jia, P. Cai and Z. Wen, *Chem. Commun.*, 2018, **54**, 2603.
25 Y. Tong, P. Chen, M. Zhang, T. Zhou, L. Zhang, W. Chu, C. Wu and Y. Xie, *ACS Catal.*, 2018, **8**, 1.
26 C. Tang, R. Zhang, W. Lu, Z. Wang, D. Liu, S. Hao, G. Du, A. M. Asiri and X. Sun, *Angew. Chem., Int. Ed.*, 2017, **56**, 842.
27 J. Wang, R. Kong, A. M. Asiri and X. Sun, *ChemElectroChem*, 2017, **4**, 481.
28 M. Liu, R. Zhang, L. Zhang, D. Liu, S. Hao, G. Du, A. M. Asiri, R. Kong and X. Sun, *Inorg. Chem. Front.*, 2017, **4**, 420.
29 B. You, N. Jiang, X. Liu and Y. Sun, *Angew. Chem., Int. Ed.*, 2016, **55**, 9913.
30 B. You, X. Liu, N. Jiang and Y. Sun, *J. Am. Chem. Soc.*, 2016, **138**, 13639.
31 N. Jiang, B. You, R. Boonstra, I. M. T. Rodriguez and Y. Sun, *ACS Energy Lett.*, 2016, **1**, 386.
32 N. Jiang, X. Liu, J. Dong, B. You, X. Liu and Y. Sun, *ChemNanoMat*, 2017, **3**, 491.
33 B. You, X. Liu, X. Liu and Y. Sun, *ACS Catal.*, 2017, **7**, 4564.
34 (*a*) S. Hao, L. Yang, D. Liu, R. Kong, G. Du, A. M. Asiri, Y. Yang and X. Sun, *Chem. Commun.*, 2017, **53**, 5710; (*b*) M. Wang, J. Ma, H. Liu, N. Luo, Z. Zhao and F. Wang, *ACS Catal.*, 2018, **8**, 2129.
35 C. Lyu, J. Zheng, R. Zhang, R. Zou, B. Liu and W. Zhou, *Mater. Chem. Front.*, 2018, **2**, 323.
36 P. Du, J. Zhang, Y. Liu and M. Huang, *Electrochem. Commun.*, 2017, **83**, 11.
37 K. E. Sanwald, T. F. Berto, W. Eisenreich, A. Jentys, O. Y. Cutiérrez and J. A. Lercher, *ACS Catal.*, 2017, **7**, 3236.
38 (*a*) W. Li, J. Liu and D. Zhao, *Nat. Rev. Mater.*, 2016, **1**, 16023; (*b*) D. He, K. Cheng, T. Peng, M. Pan and S. Mu, *J. Mater. Chem. A*, 2013, **1**, 2126; (*c*) B. You, N. Li, H. Zhu, X. Zhu and J. Yang, *ChemSusChem*, 2013, **6**, 474; (*d*) B. You, Z. Zhang, L. Zhang and J. Yang, *RSC Adv.*, 2012, **2**, 5071; (*e*) B. You, J. Yang, Y. Sun and Q. Su, *Chem. Commun.*, 2011, **47**, 12364; (*f*) B. You, L. Wang, L. Yao and J. Yang, *Chem. Commun.*, 2013, **49**, 5016; (*g*) B. You, J. Jiang and S. Fan, *ACS Appl. Mater. Interfaces*, 2014, **6**, 15302; (*h*) C. Zheng, J. Zhang, Q. Zhang, B. You and G. Chen, *Electrochim. Acta*, 2015, **152**, 216; (*i*) D. He, Y. Xiong, J. Yang, X. Chen, Z. Deng, M. Pan, Y. Li and S. Mu, *J. Mater. Chem. A*, 2017, **5**, 1930; (*j*) B. You, Y. Zhang, P. Yin, D. Jiang and Y. Sun, *Nano Energy*, 2018, **48**, 600.
39 (*a*) X. Zheng, B. Zhang, P. D. Luna, Y. Liang, R. Comin, O. Voznyy, L. Han, F. Pelayo García de Arquer, M. Liu, C. T. Dinh, T. Regier, J. J. Dynes, S. He, H. L. Xin, H. Peng, D. Prendergast, X. Du and

E. H. Sargent, *Nat. Chem.*, 2018, **10**, 149; (*b*) N. Li, D. K. Bediako, R. G. Hadt, D. Hayes, T. J. Kempa, F. Cube, D. C. Bell, L. X. Chen and D. G. Nocera, *Proc. Natl. Acad. Sci. U. S. A.*, 2017, **114**, 1486; (*c*) V. Vij, S. Sultan, A. M. Harzandi, A. Meena, J. N. Tiwari, W.-G. Lee, T. Yoon and K. S. Kim, *ACS Catal.*, 2017, **7**, 7196.

40 (*a*) J. Sanabria-Chinchilla, K. Asazawa, T. Sakamoto, K. Yamada, H. Tanaka and P. Strasser, *J. Am. Chem. Soc.*, 2011, **133**, 5425; (*b*) D. A. Finkelstein, R. Imbeault, S. Garbarino, L. Roué and D. Guay, *J. Phys. Chem. C*, 2016, **120**, 4717.

41 (*a*) H. G. Cha and K.-S. Choi, *Nat. Chem.*, 2015, **7**, 328; (*b*) P. Gallezot, *Chem. Soc. Rev.*, 2012, **41**, 1538; (*c*) Y. Kwon, K. J. P. Schouten, J. C. van der Waal, E. Jong and M. T. M. Koper, *ACS Catal.*, 2016, **6**, 6704; (*d*) M. J. Gilkey and B. Xu, *ACS Catal.*, 2016, **6**, 1420; (*e*) A. M. Robinson, J. E. Hensley and J. W. Medlin, *ACS Catal.*, 2016, **6**, 5026; (*f*) G. W. Huber, J. N. Chheda, C. J. Barrett and J. A. Dumesic, *Science*, 2005, **308**, 1446.

42 (*a*) X. Jin, M. Zhao, C. Zeng, W. Yan, Z. Song, P. S. Thapa, B. Subramaniam and R. V. Chaudhari, *ACS Catal.*, 2016, **6**, 4576; (*b*) D.-H. Nam, B. J. Taitt and K.-S. Choi, *ACS Catal.*, 2018, **8**, 1197; (*c*) S. Xu, P. Zhou, Z. Zhang, C. Yang, B. Zhang, K. Deng, S. Bottle and H. Zhu, *J. Am. Chem. Soc.*, 2017, **139**, 14775.

43 (*a*) N. Jiang, B. You, M. Sheng and Y. Sun, *Angew. Chem., Int. Ed.*, 2015, **54**, 6251; (*b*) B. You, N. Jiang, M. Sheng, S. Gul, J. Yano and Y. Sun, *Chem. Mater.*, 2015, **27**, 7636; (*c*) N. Jiang, B. You, M. Sheng and Y. Sun, *ChemCatChem*, 2016, **8**, 106; (*d*) B. You and Y. Sun, *Adv. Energy Mater.*, 2016, **6**, 1502333; (*e*) B. You, N. Jiang, M. Sheng, M. W. Bhushan and Y. Sun, *ACS Catal.*, 2016, **6**, 714; (*f*) X. Liu, B. You and Y. Sun, *ACS Sustainable Chem. Eng.*, 2017, **5**, 4778; (*g*) X. Liu, J. Dong, B. You and Y. Sun, *RSC Adv.*, 2016, **6**, 73336.

44 (*a*) J. A. Turner, *Science*, 2004, **305**, 972; (*b*) A. J. Bard and M. A. Fox, *Acc. Chem. Res.*, 1995, **28**, 141; (*c*) M. G. Walter, E. L. Warren, J. R. McKone, S. W. Boettcher, Q. Mi, E. A. Santori and N. S. Lewis, *Chem. Rev.*, 2010, **110**, 6446.

45 (*a*) H. Kim, D. Hwang, Y. Kim and J. Lee, *Chem. Commun.*, 1999, 1077; (*b*) H. Lu, J. Zhao, L. Li, L. Gong, J. Zheng, L. Zhang, Z. Wang, J. Zhang and Z. Zhu, *Energy Environ. Sci.*, 2011, **4**, 3384.

46 (*a*) Y. Ma, X. Wang, Y. Jia, X. Chen, H. Han and C. Li, *Chem. Rev.*, 2014, **114**, 9987; (*b*) Y. Xu, Y. Huang and B. Zhang, *Inorg. Chem. Front.*, 2016, **3**, 591; (*c*) K. Chang, Z. Mei, T. Wang, Q. Kang, S. Ouyang and J. Ye, *ACS Nano*, 2014, **8**, 7078.

47 A. Fujishima and K. Honda, *Nature*, 1972, **238**, 37.

48 (*a*) X. Chen, S. Shen, L. Guo and S. S. Mao, *Chem. Rev.*, 2010, **110**, 6503; (*b*) T. Hisatomi, J. Kubota and K. Domen, *Chem. Soc. Rev.*, 2014, **43**, 7520.

49 (*a*) G.-J. Ten Brink, I. W. Arends and R. A. Sheldon, *Science*, 2000, **287**, 1636; (*b*) T. Mallat and A. Baiker, *Chem. Rev.*, 2004, **104**, 3037; (*c*) S. Yurdakal, G. Palmisano, V. Loddo, V. Augugliaro and L. Palmisano, *J. Am. Chem. Soc.*, 2008, **130**, 1568.

50 (*a*) M. Zhang, Q. Wang, C. Chen, L. Zang, W. Ma and J. Zhao, *Angew. Chem., Int. Ed.*, 2009, **48**, 6081; (*b*) U. R. Pillai and E. Sahle-Demessie, *J. Catal.*, 2002, **211**, 434; (*c*) S. Yurdakal, G. Palmisano, V. Loddo, O. Alagoez, V. Augugliaro and L. Palmisano, *Green Chem.*, 2009, **11**, 510; (*d*) S. Yurdakal, G. Palmisano, V. Loddo, V. Augugliaro and L. Palmisano, *J. Am. Chem. Soc.*, 2008, **130**, 1568; (*e*) K. Imamura, H. Tsukahara, K. Hamamichi, N. Seto, K. Hashimoto and H. Kominami, *Appl. Catal., A*, 2013, **450**, 28; (*f*) M. Li, N. Zhang, R. Long, W. Ye, C. Wang and Y. Xiong, *Small*, 2017, **13**, 1604173.

51 (*a*) W. Zhai, S. Xue, A. Zhu, Y. Luo and T. Tian, *ChemCatChem*, 2011, **3**, 127; (*b*) S. Higashimoto, Y. Tanaka, R. Ishikawa, S. Hasegawa, M. Azuma, H. Ohue and Y. Sakata, *Catal. Sci. Technol.*, 2013, **3**, 400.

52 (*a*) Y. Wang, X. Wang and M. Antonietti, *Angew. Chem., Int. Ed.*, 2012, **51**, 68; (*b*) J. Liu, Y. Liu, N. Liu, Y. Han, X. Zhang, H. Huang, Y. Lifshitz, S.-T. Lee, J. Zhong and Z. Kang, *Science*, 2015, **347**, 970; (*c*) D. J. Martin, P. J. T. Reardon, S. J. A. Moniz and J. Tang, *J. Am. Chem. Soc.*, 2014, **136**, 12568.

53 F. Li, Y. Wang, J. Du, Y. Zhu, C. Xu and L. Sun, *Appl. Catal., B*, 2018, **225**, 258.

54 Y. Liu, S. Yang, S.-N. Yin, L. Feng, Y. Zang and H. Xue, *Chem. Eng. J.*, 2018, **334**, 2401.

55 H. Kasap, C. A. Caputo, B. C. M. Martindale, R. Godin, V. W. Lau, B. V. Lotsch, J. R. Durrant and E. Reisner, *J. Am. Chem. Soc.*, 2016, **138**, 9183.

56 (*a*) K. Akihiko and Y. Miseki, *Chem. Soc. Rev.*, 2009, **38**, 253; (*b*) Z. Chai, T.-T. Zeng, Q. Li, L.-Q. Lu, W.-J. Xiao and D. Xu, *J. Am. Chem. Soc.*, 2016, **138**, 10128.

57 T. Mitkina, C. Stanglmair, W. Setzer, M. Gruber, H. Kisch and B. König, *Org. Biomol. Chem.*, 2012, **10**, 3556.

58 T. Simon, N. Bouchonville, M. J. Berr, A. Vaneski, A. Adrović, D. Volbers, R. Wyrwich, M. Döblinger, A. S. Susha, A. L. Rogach, F. Jäckel, J. K. Stolarczyk and J. Feldmann, *Nat. Mater.*, 2014, **13**, 1013.

59 (*a*) T. P. A. Ruberu, N. C. Nelson, I. I. Slowing and J. Vela, *J. Phys. Chem. Lett.*, 2012, **3**, 2798; (*b*) D. Jiang, X. Chen, Z. Zhang, L. Zhang, Y. Wang, Z. Sun, R. M. Irfan and P. Du, *J. Catal.*, 2018, **357**, 147.

60 D. W. Wakerley, M. F. Kuehnel, K. L. Orchard, K. H. Ly, T. E. Rosser and E. Reisner, *Nat. Energy*, 2017, **2**, 17021.

61 (*a*) R. F. Service, *Science*, 2009, **324**, 875; (*b*) X. Huang, S. Li, Y. Huang, S. Wu, X. Zhou, S. Li, C. L. Gan, F. Boey, C. A. Mirkin and H. Zhang, *Nat. Commun.*, 2011, **2**, 292; (*c*) K. G. Zhou, N. N. Mao, H. X. Wang, Y. Peng and H. L. Zhang, *Angew. Chem., Int. Ed.*, 2011, **50**, 10839.

62 (*a*) Y. Xu, W. Zhao, R. Xu, Y. Shi and B. Zhang, *Chem. Commun.*, 2013, **49**, 9803; (*b*) Y. Huang, Y. Xu, J. Zhang, X. Yin, Y. Guo and B. Zhang, *J. Mater. Chem. A*, 2015, **3**, 19057.

63 G. Han, Y.-H. Jin, R. A. Burgess, N. E. Dickenson, X.-M. Cao and Y. Sun, *J. Am. Chem. Soc.*, 2017, **139**, 15584.

64 P. V. Kamat, K. Tvrdy, D. R. Baker and J. G. Radich, *Chem. Rev.*, 2010, **110**, 6664.

65 L.-M. Zhao, Q.-Y. Meng, X.-B. Fan, C. Ye, X.-B. Li, B. Chen, V. Ramamurthy, C.-H. Tung and L.-Z. Wu, *Angew. Chem., Int. Ed.*, 2017, **56**, 3020.

66 S. Sarina, S. Bai, Y. Huang, C. Chen, J. Jia, E. Jaatinen, G. A. Ayoko, Z. Bao and H. Zhu, *Green Chem.*, 2014, **16**, 331.

67 Z. Liu, J. Caner, A. Kudo, H. Naka and S. Saito, *Chem. – Eur. J.*, 2013, **19**, 9452.

68 Z. Liu, Z. Yin, C. Cox, M. Bosman, X. Qian, N. Li, H. Zhao, Y. Du, J. Li and D. G. Nocera, *Sci. Adv.*, 2016, **2**, e1501425.